Unravelling the ion transport and the interphase properties of a mixed olivine cathode for Na-ion battery

Luca Minnetti[a], Leonardo Sbrascini[a], Antunes Staffolani[a,b], Vittorio Marangon[c,d], Francesco Nobili[a,e,*], and Jusef Hassoun[c,d,f,*]

[a] *School of Sciences and Technologies – Chemistry Division, University of Camerino, Via Madonna delle Carceri ChIP, 62032, Camerino, Italy.*

[b] *Current affiliation: University of Bologna, Department of Chemistry "Giacomo Ciamician", Via Francesco Selmi 2, 40126, Bologna, Italy.*

[c] *Graphene Labs, Istituto Italiano di Tecnologia, via Morego 30, Genoa, 16163, Italy.*

[d] *Department of Chemical, Pharmaceutical and Agricultural Sciences, University of Ferrara, Via Fossato di Mortara 17, 44121, Ferrara, Italy.*

[e] *GISEL – Centro di Riferimento Nazionale per i Sistemi di Accumulo Elettrochimico di Energia, INSTM, Firenze 50121, Italy*

[f] *National Interuniversity Consortium of Materials Science and Technology (INSTM) University of Ferrara Research Unit, University of Ferrara, Via Fossato di Mortara, 17, 44121, Ferrara, Italy.*

*Corresponding authors: francesco.nobili@unicam.it, jusef.hassoun@unife.it

Supplementary Material

Fig. S1 shows the morphological features of LFMP (images in panels a–h), FMP (images in panels i–p), and NFMP (images in panels q–y) electrodes obtained by SEM-EDS analysis (see the Manuscript for samples' acronyms). The related SEM images at different magnification indicate for the three samples the presence of agglomerates of micrometric secondary particles formed by sub-micrometric primary particles homogeneously blended into the electrode film, as expected by the SEM images related to LFMP powder reported in a previous work (see Experimental section in the Manuscript for details on electrode preparation) [1].

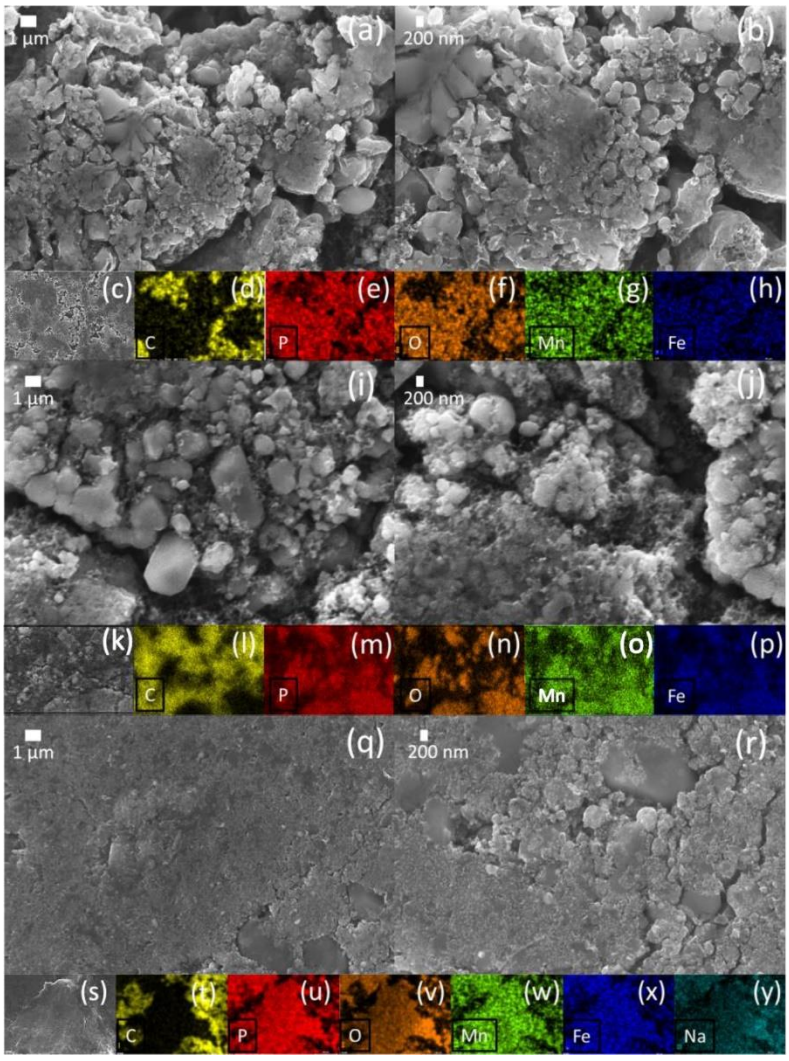

Fig. S1. SEM and EDS analyses of (a–h) LFMP, (i–p) FMP, and (q–y) NFMP electrodes. In detail: SEM images at different magnifications for (a–c) LFMP, (i–k) FMP, and (q–s) NFMP; SEM-EDS elemental maps of (d,l,t) C, (e,m,u) P, (f,n,v) O, (g,o,w) Mn, (h,p,x) Fe, and (y) Na for (d-h) LFMP, (l-p) FMP, and (t-y) NFMP. See the Manuscript for acronyms.

Fig. S2 reports the CV measurement performed at a scan rate of 0.02 mV s^{-1} on the Na|EC:PC 1:1 v/v 1 M $NaPF_6$ + 2% FEC|NFMP three-electrode cell to determine all the electrochemical processes ascribed to the Fe^{3+}/Fe^{2+} and Mn^{3+}/Mn^{2+} redox couples. The CV response indicates the occurrence of two oxidation processes revealed by peaks centered at about 3.05 and 3.16 V vs. Na^+/Na and 3.85 V vs. Na^+/Na during the anodic scan, which are almost completely reversed into two reduction processes with peaks at about 2.82, 3.02, and 3.55 V vs. Na^+/Na during cathodic scan, the first two convoluted signals ascribed to the Fe^{3+}/Fe^{2+} redox couple and the latter to the Mn^{3+}/Mn^{2+} redox couple, respectively [2]. See the Results and Discussion section of Fig. 2(a) in the Manuscript for further details.

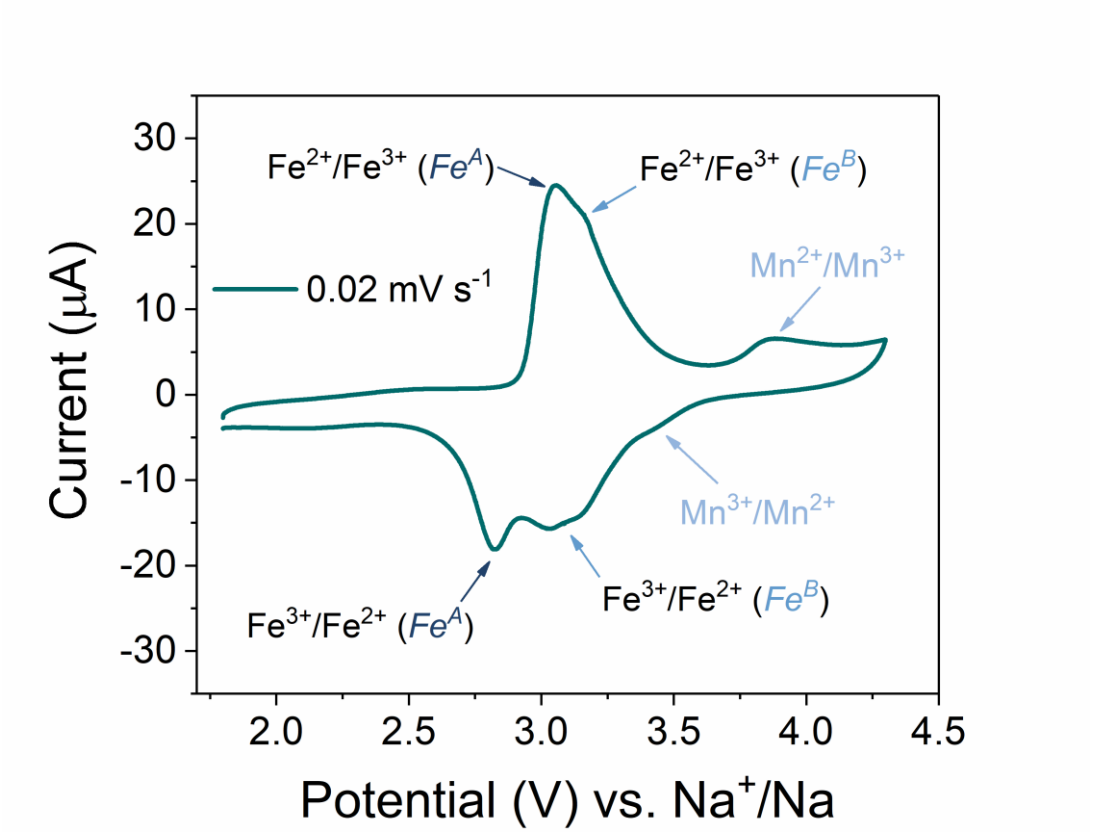

Fig. S2. CV of the Na|EC:PC 1:1 v/v, 1M $NaPF_6$ + 2% FEC w/w|NFMP three-electrode cell with a Na reference electrode (peaks with related redox couples reactions are indicated). CV potential range: 1.8 – 4.3 V vs. Na^+/Na; scan rate: 0.02 mV s^{-1}. Room temperature (25 °C). See the Manuscript for acronyms.

Table S1 reports the crystallographic details of the NFMP cathode obtained through Rietveld refinement of the diffractogram shown in Fig. 1(c) in the Manuscript, in order to evaluate the degree of Na/Mn antisite mixing. The table shows a cation disorder of about 8%, particularly ascribed to Mn^{2+}, and partially justifies the limited contribution of the Mn^{3+}/Mn^{2+} redox couple to the cell capacity [3]. See the Results and Discussion section of Fig. 2(c–d) in the Manuscript for further details.

Atom	Wycoff position	*x*	*y*	*z*	Occupancy	B_{iso} (Å^2)
Na1	4a	0	0	0	0.918(6)	0.038(7)
Na2	4c	0.2852(6)	0.25	-0.0086(2)	0.084(0)	0.018(8)
Mn1	4a	0	0	0	0.073(3)	0.038(7)
Mn2	4c	0.2852(6)	0.25	-0.0086(2)	0.326(7)	0.018(8)
Fe1	4a	0	0	0	0.009(4)	0.038(7)
Fe2	4c	0.2852(6)	0.25	-0.0086(2)	0.590(6)	0.018(8)
P1	4c	0.1073(4)	0.25	0.4409(1)	1.0	0.033(3)
O1	4c	0.1124(7)	0.25	0.1471(9)	1.0	0.005(6)
O2	4c	0.4675(2)	0.25	0.1609(5)	1.0	0.009(9)
O3	8d	0.1733(6)	0.0609(5)	0.3104(5)	1.0	0.011(1)

Table S1. Crystallographic details and atomic parameters of the NFMP cathode obtained from Rietveld refinement of Fig. 1(c) in the Manuscript. See the Manuscript for acronyms.

Fig. S3 reveals the structural and morphological retention of the NFMP electrode upon prolonged cycling in sodium cell reported in Fig. 2(e,f) in the Manuscript. Fig. S3(a) shows the XRD analysis of the pristine and the cycled electrodes, compared with a reference sample (ICSD # 26006) [4]. Hence, the XRD patterns of both electrodes exhibit a defined crystalline structure, in full agreement with the one observed in Fig. 1(b,c) in the Manuscript for NFMP electrode, thus indicating the retention of the single-phase olivine structure, with more defined peaks of the cycled electrode likely ascribed to the different loading of the samples as indicated by the intensity of the Al current collector peak in the diffractograms. Moreover, the morphology of the pristine (Fig. S3b,c) and the cycled (Fig. S3d,e) electrodes is studied by SEM. For the pristine electrode, SEM images show submicrometric primary particles aggregated into micrometric secondary particles. The cycled electrode reflects

almost unaltered aspect without relevant reorganization of the NFMP domains despite long cycling in sodium cell. Furthermore, the presence for the cycled electrode of different domains with rough morphology, which are not observed in the pristine sample (compare Fig. S3b,c and Fig. S3d,e), as well as dispersed glass fibers due to the electrolyte separator, is related to the formation of a SPI passivation layer during cycling as reported in previous works [1,5]. See Experimental section in the Manuscript for electrode preparation and cell assembly, and Fig. 2(e,f) for related galvanostatic cycles.

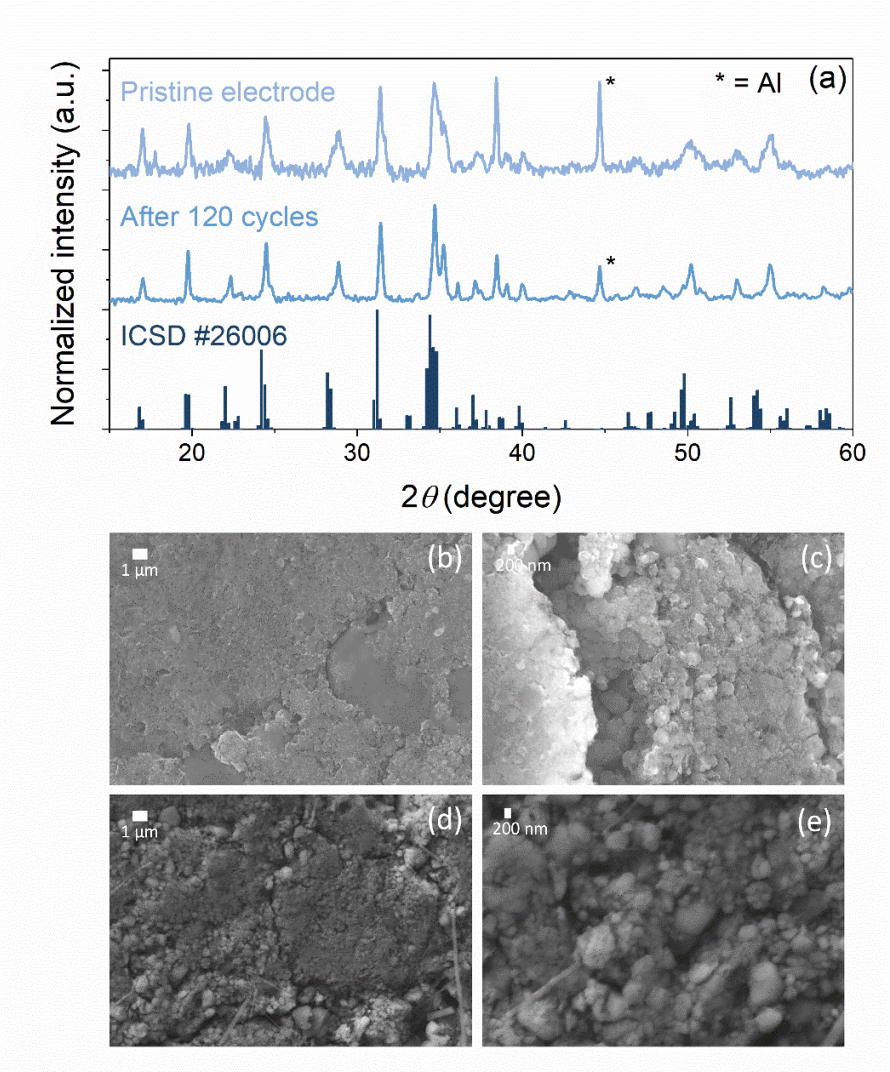

Fig. S3. (a) Comparison between the XRD patterns of a pristine NFMP electrode, the NFMP electrode recovered upon the galvanostatic cycling measurement in sodium cell reported in Fig. 2(e,f) of the Manuscript, and the reference diffractogram (ICSD #26006). (b–e) SEM images at different magnifications of (b–c) the pristine NFMP electrode and (d–e) the NFMP electrode recovered upon the galvanostatic cycling measurement in sodium cell reported in Fig. 2(e,f) of the Manuscript. See the Manuscript for acronyms.

The measured values of peak current related with the electrochemical processes of LFMP and NFMP in CV experiments (Fig. 4a and Fig. 4b in the Manuscript, respectively) have been reported versus the square root of the scan rate and displayed in Fig. S4. The points of Fig. S4 follow a linear trend as expected by the reversible redox processes, and confirmed by coefficient of determination (R^2) values. The slope values, $dI_p/dv^{1/2}$, have been used to calculate the Li^+ and the Na^+ diffusion coefficient, D_{CV} ($cm^2\ s^{-1}$), according to the Randles-Sevcik equation (see the Results and Discussion section, Eq. (1) in the Manuscript).

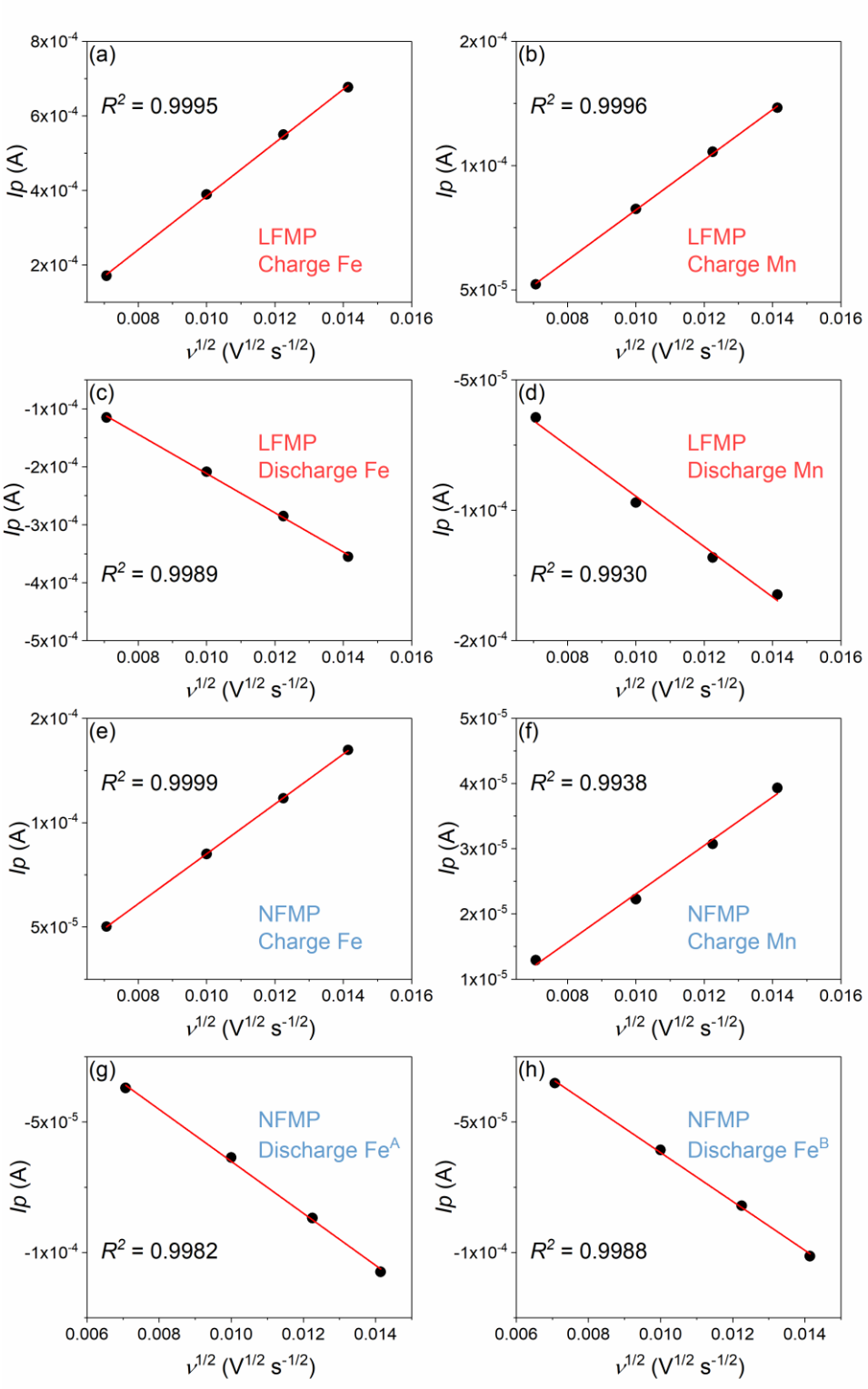

Fig. S4. Peak current (I_p, A) vs. square root of scan rate ($\nu^{1/2}$, V$^{1/2}$ s$^{-1/2}$) and related linear fit, with associated coefficient of determination (R^2) values, corresponding to the Fe^{3+}/Fe^{2+} and Mn^{3+}/Mn^{2+} processes within the olivine structure of LFMP and NFMP as determined by CV in Fig. 4(a) and Fig. 4(b) in the Manuscript, respectively. See the Manuscript for acronyms.

Fig. S5 shows the galvanostatic profiles of LFMP (Fig. S5a) and NFMP (Fig. S5b) during three activation cycles in sodium cell at C/10 current (1C = 170 mA g^{-1}) for LFMP and at C/20 current (1C = 154 mA g^{-1}) for NFMP, carried out before GITT experiments of Fig. 5 in the Manuscript. The galvanostatic profiles show limited polarization for both the samples with a discharge capacity at the 3rd cycle of about 118 mAh g^{-1} and 88 mAh g^{-1} for LFMP and NFMP, respectively.

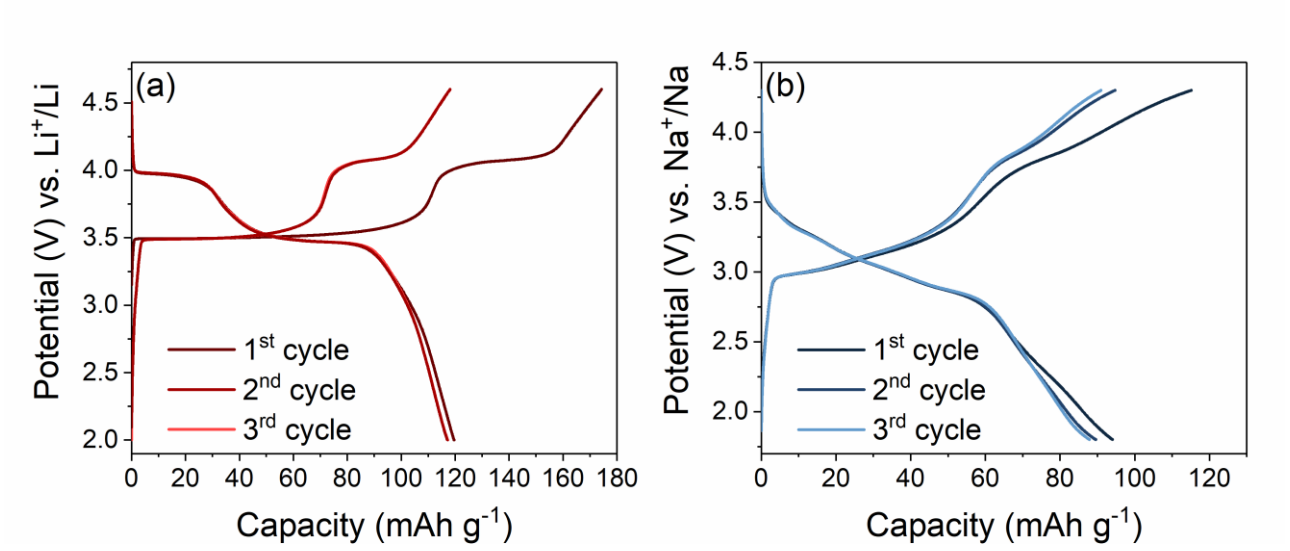

Fig. S5. Voltage profiles of the first three galvanostatic activation cycles performed before GITT for (a) LFMP and (b) NFMP samples used as working electrodes in three-electrode cells with (a) lithium metal foils or (b) sodium metal foils as the counter and reference electrodes. Tests performed at (a) C/10 rate (1C = 170 mA g^{-1}) and at (b) C/20 rate (1C = 154 mA g^{-1}). Room temperature (25 °C). See the Manuscript for acronyms and Fig. 5 for corresponding GITT.

Fig. S6(a) and Fig. S6(b) respectively show the potential profile of a single GITT step obtained from LFMP in lithium three-electrode cell at x = 0.55 in $Li_{1-x}Fe_{0.6}Mn_{0.4}PO_4$ (from Fig. 5a in the Manuscript), and from NFMP in sodium three-electrode cell at x = 0.23 in $Na_{1-x}Fe_{0.6}Mn_{0.4}PO_4$ (from Fig. 5b in the Manuscript). The potential quickly increases through application of the square current pulse (17 mA g^{-1} for LFMP and 7.7 mA g^{-1} for NFMP), and decreases at quasi-equilibrium value (E_0) after cell relaxation at open circuit voltage (OCV). E_0 values have been used to calculate dE/dx for D_{GITT} determination in Fig. 5(e) in the Manuscript. Indeed, the measured potential of each GITT pulse has been plotted as a function of the square root of the time as exemplified in Fig. S6(c) for LFMP

and Fig. 6(d) for NFMP, and the slope values of the obtained linear plots ($dE/dt^{1/2}$) have been used to determine D_{GITT}, according to the Eq. (2) in the manuscript. See Experimental and Results and Discussion sections of the Manuscript.

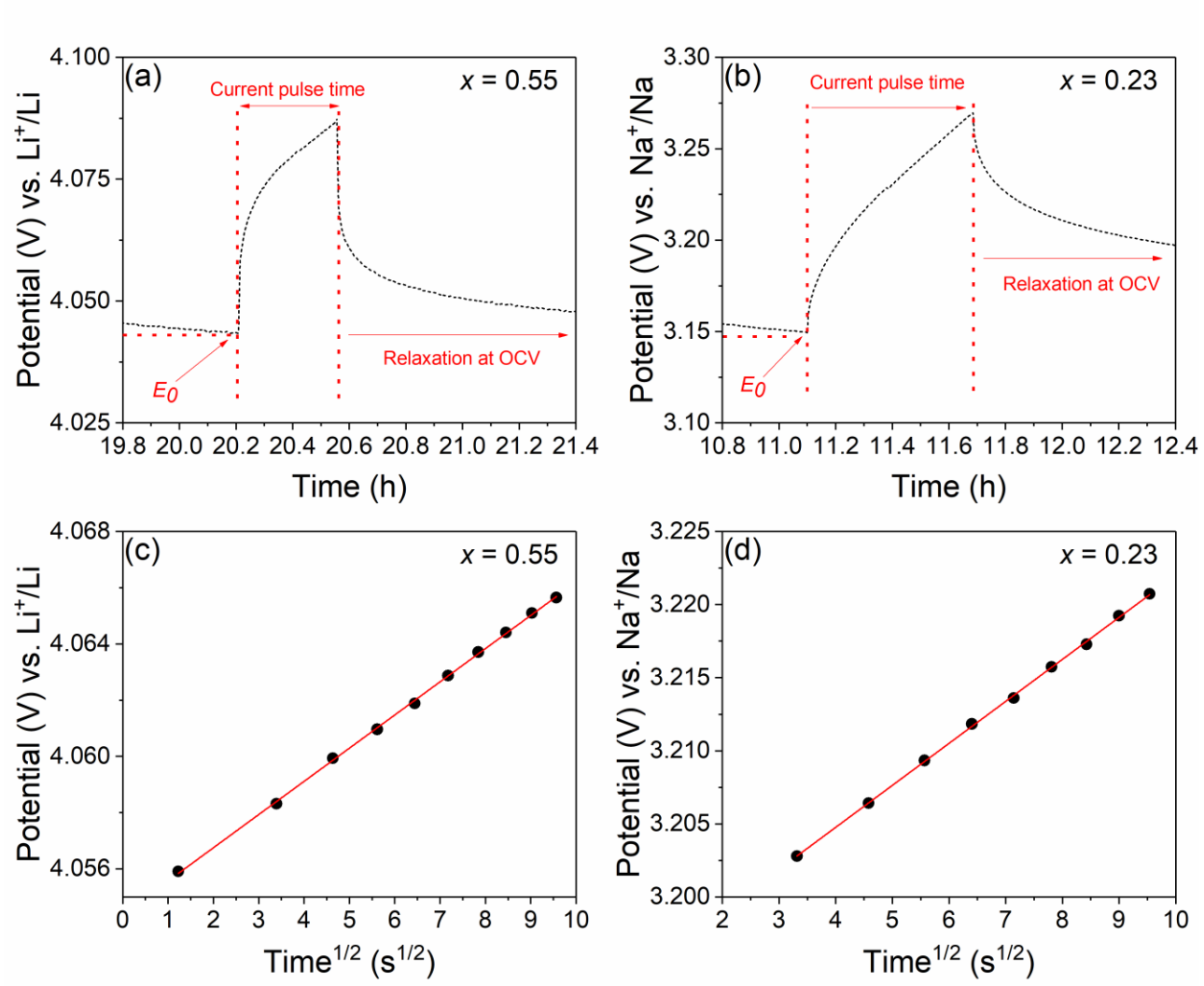

Fig. S6. Example of a single GITT step obtained for (a) LFMP at $x = 0.55$ in $Li_{1-x}Fe_{0.6}Mn_{0.4}PO_4$ (from Fig. 5a in the Manuscript) and (b) NFMP at $x = 0.23$ in $Na_{1-x}Fe_{0.6}Mn_{0.4}PO_4$ (from Fig. 5b in the Manuscript). GITT experiments have been performed applying square current pulses of 17 mA g^{-1} during 1249.5 s and square current pulses of 7.7 mA g^{-1} during 2107.5 s, followed by potential relaxation steps of 1 hour at OCV, for LFMP and NFMP, respectively. Potential vs. time$^{1/2}$ and related linear fit from GITT of (c) LFMP at $x = 0.55$ in $Li_{1-x}Fe_{0.6}Mn_{0.4}PO_4$ and (d) NFMP at $x = 0.23$ in $Na_{1-x}Fe_{0.6}Mn_{0.4}PO_4$. See the Manuscript for acronyms and Fig. 5(e) for the obtained D_{GITT}.

Table S2 reports D_{GITT} values calculated through Eq. (2) shown in Fig. 5(e) (red) in the Manuscript, during de-lithiation and lithiation for LFMP. The D values are reported with the corresponding E_0 and exchanged lithium ions (x) in $Li_{1-x}Fe_{0.6}Mn_{0.4}PO_4$.

De-Lithiation			**Lithiation**		
E_0 (V vs. Li^+/Li)	x in $Li_{1-x}Fe_{0.6}Mn_{0.4}PO_4$	D_{GITT} (cm^2 s^{-1})	E_0 (V vs. Li^+/Li)	x in $Li_{1-x}Fe_{0.6}Mn_{0.4}PO_4$	D_{GITT} (cm^2 s^{-1})
3.47	0.03	1.9×10^{-14}	4.06	0.66	8.3×10^{-13}
3.48	0.07	6.1×10^{-12}	4.03	0.62	1.9×10^{-12}
3.48	0.10	4.4×10^{-12}	4.03	0.59	1.2×10^{-11}
3.48	0.14	5.9×10^{-12}	4.03	0.56	1.8×10^{-10}
3.48	0.17	2.4×10^{-11}	4.02	0.52	1.3×10^{-9}
3.48	0.21	1.7×10^{-10}	4.00	0.49	1.1×10^{-10}
3.49	0.24	5.0×10^{-10}	3.93	0.45	3.8×10^{-10}
3.50	0.28	5.7×10^{-10}	3.64	0.42	5.4×10^{-10}
3.51	0.31	1.4×10^{-9}	3.55	0.38	6.1×10^{-10}
3.53	0.35	2.2×10^{-9}	3.52	0.35	6.2×10^{-10}
3.56	0.38	3.4×10^{-9}	3.50	0.31	4.2×10^{-10}
3.63	0.42	1.6×10^{-8}	3.48	0.28	8.3×10^{-11}
3.91	0.45	3.5×10^{-9}	3.48	0.24	2.1×10^{-11}
4.02	0.49	7.5×10^{-11}	3.47	0.21	1.1×10^{-11}
4.04	0.52	5.0×10^{-11}	3.47	0.17	1.0×10^{-11}
4.05	0.56	2.0×10^{-12}	3.47	0.14	1.5×10^{-11}
4.05	0.59	3.7×10^{-13}	3.47	0.10	2.7×10^{-10}
4.05	0.63	3.9×10^{-13}	3.47	0.07	9.9×10^{-11}
4.05	0.66	5.5×10^{-13}	3.46	0.03	6.2×10^{-11}
4.06	0.69	3.0×10^{-13}	/	/	/

Table S2. Quasi-equilibrium potentials (E_0), exchanged lithium ions (x) in $Li_{1-x}Fe_{0.6}Mn_{0.4}PO_4$, and D values calculated through GITT (see Eq. (2) in the Manuscript) for three-electrodes Li|LFMP cell during de-lithiation and lithiation processes. See the Manuscript for acronyms and Fig. 5(e) for the trends of D_{GITT}.

Table S3 reports the D_{GITT} values, calculated through Eq. (2) and shown in Fig. 5(e) (blue) in the Manuscript, during de-sodiation and sodiation for NFMP. The *D* values are reported with the corresponding E_0 and exchanged sodium ions (*x*) in $Na_{1-x}Fe_{0.6}Mn_{0.4}PO_4$.

De-Sodiation			**Sodiation**		
E_0 (V vs. Na^+/Na)	*x* in $Na_{1-x}Fe_{0.6}Mn_{0.4}PO_4$	D_{GITT} ($cm^2\ s^{-1}$)	E_0 (V vs. Na^+/Na)	*x* in $Na_{1-x}Fe_{0.6}Mn_{0.4}PO_4$	D_{GITT} ($cm^2\ s^{-1}$)
2.93	0.03	2.3×10^{-14}	3.58	0.50	6.4×10^{-14}
2.95	0.06	5.6×10^{-12}	3.55	0.47	2.0×10^{-13}
2.98	0.09	1.6×10^{-11}	3.51	0.44	4.7×10^{-13}
3.03	0.12	1.7×10^{-11}	3.44	0.41	9.8×10^{-13}
3.08	0.15	1.6×10^{-11}	3.35	0.38	2.3×10^{-12}
3.11	0.17	2.4×10^{-11}	3.28	0.35	6.0×10^{-12}
3.15	0.20	2.9×10^{-11}	3.22	0.32	1.3×10^{-11}
3.19	0.23	2.3×10^{-11}	3.17	0.29	1.3×10^{-11}
3.25	0.26	2.6×10^{-11}	3.12	0.26	1.2×10^{-11}
3.32	0.29	4.2×10^{-11}	3.09	0.24	2.0×10^{-11}
3.47	0.32	1.7×10^{-11}	3.06	0.21	2.2×10^{-11}
3.63	0.35	3.0×10^{-12}	3.02	0.18	2.3×10^{-11}
3.69	0.38	2.4×10^{-13}	2.99	0.15	1.3×10^{-11}
3.70	0.41	4.3×10^{-14}	2.95	0.12	1.1×10^{-11}
3.72	0.44	4.4×10^{-14}	2.92	0.09	4.4×10^{-12}
3.73	0.47	4.0×10^{-14}	2.91	0.06	1.4×10^{-12}
3.75	0.49	3.0×10^{-14}	2.90	0.03	6.5×10^{-13}
3.76	0.51	2.0×10^{-14}	2.89	0.01	2.6×10^{-13}

Table S3. Quasi-equilibrium potentials (E_0), exchanged sodium ions (*x*) in $Na_{1-x}Fe_{0.6}Mn_{0.4}PO_4$, and *D* values calculated through GITT (see Eq. (2) in the Manuscript) for three-electrodes Na|NFMP cell during de-sodiation and sodiation processes. See the Manuscript for acronyms and Fig. 5(e) for the trends of D_{GITT}.

Fig. S7 reports the Nyquist plots upon de-lithiation (Fig. S7a) and lithiation (Fig. S7b) from the staircase electrochemical impedance spectroscopy (SPEIS) analysis of the LFMP electrode performed at the 3rd cycle in lithium cell. The impedance plots are collected every 40 mV in order to evaluate all the electrochemical processes occurring at the interfaces. These spectra are fitted through the non-linear least squares (NLLS) method [6,7] using the RelaxIS3 software focusing on the low-frequency diffusion region which was subtracted for the calculation of distribution of relaxation times (DRT). The Nyquist plots without diffusion contributions are reported in Fig. 6 of the Manuscript. The NLLS fit is performed using the equivalent circuit $R_e(R_iQ_i)WQ_w$ including the electrolyte

resistance as high-frequency intercept of the plot with the real axis (R_e), in series with three resistances and constant phase elements accounting for the interphase associated to SEI formation and charge transfer of the electrodes (R_iQ_i) semicircles at medium frequency, and a Warburg element in series with solid state diffusion element at low-frequency to simulate both transmissive and reflective boundaries (WQ_w) See the Experimental section and Fig. 6 in the Manuscript for further details and data.

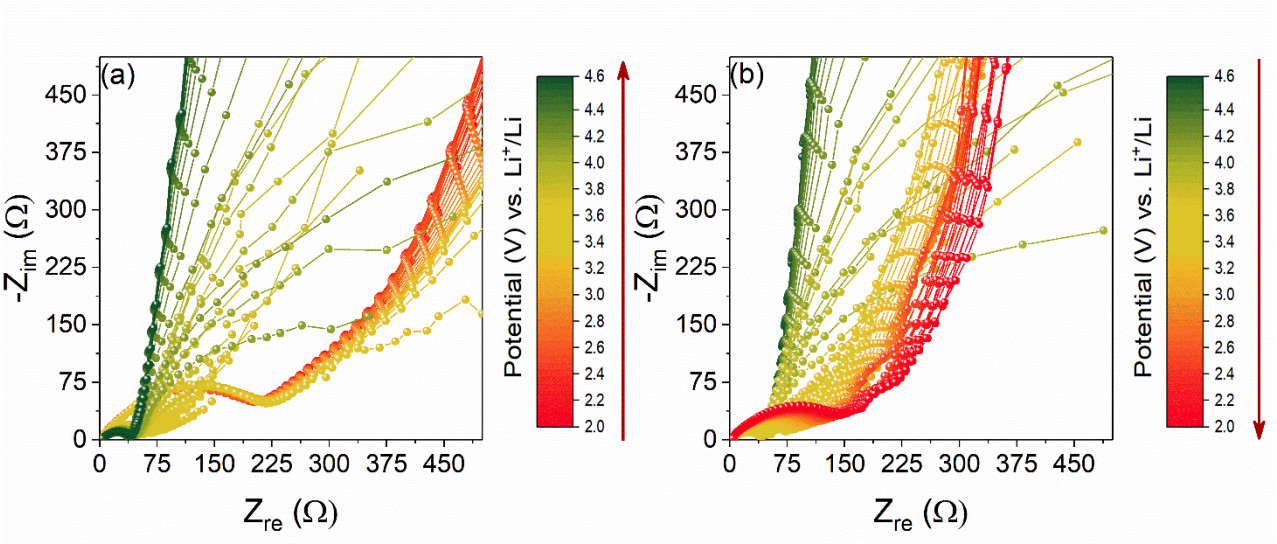

Fig. S7. Nyquist plots obtained during (a) de-lithiation and (b) lithiation from the staircase electrochemical impedance spectroscopy (SPEIS) analysis of LFMP electrode performed at the 3rd cycle. EIS collected every 40 mV; potential range: 2.0 – 4.6 V vs. Li^+/Li; frequency range: 200 kHz – 10 mHz; alternate voltage signal: 10 mV. See the Experimental section and Fig. 6 in the Manuscript for the related experiment and data.

The Nyquist plots upon charge and discharge of LFMP in lithium cell of Fig. 6(a) and Fig. 6(c) in the Manuscript are analyzed by NLLS method using a RelaxIS3 software (only fits with χ^2 values of the order of 10^{-4} or lower were considered) [6,7] and the results are reported in Table S4 and Table S5, respectively, to obtain the R_{ct} trend associated to the charge transfer resistance of LFMP, as reported in Fig. 6(e) in the Manuscript. The NLLS fits are performed with the equivalent circuit $R_e(R_{cont}Q_{cont})(R_{Li}Q_{Li})(R_{ct}Q_{ct})$ including the electrolyte resistance as high-frequency intercept of the plot with the real axes (R_e), in series with three resistances and constant phase elements accounting for: the contact resistance semicircle at higher frequency, related with cables and to the

particles/current collector contact (R_{cont}); the interphase resistance semicircle at medium-high frequency, related with the SEI and SPI formation at the electrodes and to lithium charge transfer (R_{Li}); and the other interphase resistance semicircle at lower frequency, related with the LFMP charge transfer (R_{ct}).

Potential (V vs. Li^+/Li)	R_{cont} (Ω)	R_{Li} (Ω)	R_{ct} (Ω)	χ^2
2.00	18 ± 3	187 ± 4	135 ± 2	4×10^{-4}
2.04	19 ± 2	181 ± 3	127 ± 2	3×10^{-4}
2.08	20 ± 2	179 ± 2	125 ± 1	2×10^{-4}
2.12	20 ± 2	179 ± 3	112 ± 1	2×10^{-4}
2.16	19 ± 2	180 ± 3	105 ± 1	2×10^{-4}
2.20	19 ± 2	180 ± 2	108 ± 1	2×10^{-4}
2.24	18 ± 2	181 ± 2	97 ± 1	2×10^{-4}
2.28	18 ± 2	181 ± 2	97 ± 1	2×10^{-4}
2.32	16 ± 2	183 ± 2	97 ± 1	2×10^{-4}
2.36	16 ± 2	183 ± 2	96 ± 1	2×10^{-4}
2.40	17 ± 2	184 ± 2	101 ± 1	2×10^{-4}
2.44	15 ± 2	184 ± 2	98 ± 1	2×10^{-4}
2.48	15 ± 2	186 ± 2	96 ± 1	2×10^{-4}
2.52	15 ± 2	186 ± 2	94 ± 1	2×10^{-4}
2.56	15 ± 1	187 ± 2	91 ± 1	2×10^{-4}
2.60	16 ± 2	187 ± 2	89 ± 1	2×10^{-4}
2.64	17 ± 2	185 ± 3	98 ± 2	2×10^{-4}
2.68	15 ± 2	190 ± 2	92 ± 1	2×10^{-4}
2.72	14 ± 2	194 ± 2	87 ± 1	2×10^{-4}
2.76	12 ± 2	200 ± 3	81 ± 2	4×10^{-4}
2.80	11 ± 2	204 ± 4	75 ± 2	8×10^{-4}
2.84	11 ± 2	206 ± 3	72 ± 2	7×10^{-4}
2.88	11 ± 2	207 ± 3	70 ± 2	5×10^{-4}
2.92	10 ± 2	210 ± 3	67 ± 2	8×10^{-4}
2.96	10 ± 2	209 ± 3	66 ± 2	5×10^{-4}
3.00	10 ± 2	211 ± 3	63 ± 2	6×10^{-4}
3.04	9 ± 2	212 ± 3	62 ± 3	7×10^{-4}
3.08	9 ± 2	212 ± 3	63 ± 3	8×10^{-4}
3.12	10 ± 2	210 ± 4	64 ± 3	8×10^{-4}
3.16	10 ± 2	211 ± 3	64 ± 3	8×10^{-4}
3.20	10 ± 2	209 ± 3	65 ± 3	8×10^{-4}
3.24	11 ± 2	209 ± 3	64 ± 3	8×10^{-4}
3.28	10 ± 2	209 ± 4	63 ± 3	9×10^{-4}
3.32	10 ± 2	207 ± 4	61 ± 3	1×10^{-4}
3.36	11 ± 2	208 ± 4	60 ± 3	1×10^{-4}
3.40	12 ± 2	205 ± 3	60 ± 2	6×10^{-4}
3.44	11 ± 2	207 ± 4	56 ± 3	1×10^{-4}
3.48	16 ± 3	189 ± 4	59 ± 3	9×10^{-4}
3.52	9 ± 1	55 ± 1	7 ± 1	5×10^{-5}
3.56	9 ± 1	45 ± 1	6 ± 1	6×10^{-5}
3.60	8 ± 1	42 ± 1	6 ± 1	4×10^{-5}
3.64	8 ± 1	40 ± 1	7 ± 1	5×10^{-5}
3.68	8 ± 1	40 ± 1	8 ± 1	5×10^{-5}
3.72	8 ± 1	39 ± 1	9 ± 1	6×10^{-5}
3.76	8 ± 1	39 ± 1	10 ± 1	4×10^{-5}

3.80	8 ± 1	38 ± 1	10 ± 1	3×10^{-5}
3.84	8 ± 1	38 ± 1	10 ± 1	3×10^{-5}
3.88	8 ± 1	38 ± 1	10 ± 1	3×10^{-5}
3.92	8 ± 1	38 ± 1	10 ± 1	3×10^{-5}
3.96	8 ± 1	38 ± 1	9 ± 1	4×10^{-5}
4.00	8 ± 1	37 ± 1	9 ± 1	4×10^{-5}
4.04	7 ± 1	36 ± 1	8 ± 1	7×10^{-5}
4.08	7 ± 1	32 ± 1	5 ± 1	4×10^{-5}
4.12	7 ± 1	30 ± 1	5 ± 1	4×10^{-5}
4.16	6 ± 1	30 ± 1	5 ± 1	4×10^{-5}
4.20	7 ± 2	28 ± 3	23 ± 2	2×10^{-4}
4.24	6 ± 1	29 ± 1	24 ± 1	4×10^{-4}
4.28	6 ± 1	28 ± 1	25 ± 1	4×10^{-4}
4.32	7 ± 1	28 ± 1	26 ± 1	3×10^{-4}
4.36	7 ± 1	28 ± 1	27 ± 1	3×10^{-4}
4.40	8 ± 1	27 ± 1	29 ± 1	2×10^{-4}
4.44	8 ± 1	27 ± 1	30 ± 1	2×10^{-4}
4.48	9 ± 1	27 ± 1	32 ± 1	2×10^{-4}
4.52	9 ± 1	27 ± 1	33 ± 1	1×10^{-4}
4.56	10 ± 1	28 ± 1	35 ± 1	1×10^{-4}
4.60	10 ± 1	28 ± 1	37 ± 1	1×10^{-4}

Table S4. Contact resistance (R_{cont}), interphase resistance mainly related with lithium SEI and charge transfer (R_{Li}), charge transfer resistance associated with LFMP (R_{ct}), and chi-square value indicating the accuracy (χ^2) of the NLLS [6,7] analysis using the equivalent circuit $R_e(R_{cont}Q_{cont})(R_{Li}Q_{Li})(R_{ct}Q_{ct})$ on the impedance data obtained from SPEIS measurement of the Li|LFMP cell during charge process. See Fig. 6(a) in the Manuscript for related Nyquist plots.

Potential (V vs. Li^+/Li)	R_{cont} (Ω)	R_{Li} (Ω)	R_{ct} (Ω)	χ^2
4.60	7 ± 2	33 ± 2	27 ± 1	2×10^{-4}
4.56	8 ± 3	32 ± 3	35 ± 2	3×10^{-4}
4.52	12 ± 4	27 ± 4	47 ± 3	4×10^{-4}
4.48	13 ± 5	26 ± 5	52 ± 4	5×10^{-4}
4.44	8 ± 3	33 ± 4	50 ± 3	4×10^{-4}
4.40	9 ± 3	33 ± 4	52 ± 3	4×10^{-4}
4.36	9 ± 2	33 ± 4	52 ± 3	4×10^{-4}
4.32	8 ± 2	34 ± 4	51 ± 3	5×10^{-4}
4.28	15 ± 3	26 ± 6	55 ± 4	7×10^{-4}
4.24	9 ± 2	34 ± 4	44 ± 2	4×10^{-4}
4.20	15 ± 3	26 ± 6	51 ± 4	6×10^{-4}
4.16	8 ± 2	35 ± 4	39 ± 2	4×10^{-4}
4.12	9 ± 3	34 ± 4	36 ± 2	3×10^{-4}
4.08	17 ± 4	23 ± 6	43 ± 4	7×10^{-4}
4.04	17 ± 4	24 ± 6	43 ± 5	7×10^{-4}
4.00	8 ± 2	37 ± 4	27 ± 2	4×10^{-4}
3.96	8 ± 3	34 ± 3	20 ± 1	3×10^{-4}
3.92	8 ± 3	31 ± 3	20 ± 1	3×10^{-4}
3.88	10 ± 2	29 ± 2	20 ± 1	1×10^{-4}
3.84	9 ± 3	30 ± 3	21 ± 1	3×10^{-4}
3.80	10 ± 2	29 ± 3	21 ± 1	2×10^{-4}
3.76	9 ± 3	30 ± 3	19 ± 1	2×10^{-4}
3.72	8 ± 3	32 ± 3	15 ± 1	3×10^{-4}

3.68	10 ± 3	30 ± 3	12 ± 1	2×10^{-4}
3.64	11 ± 2	28 ± 2	10 ± 1	1×10^{-4}
3.60	11 ± 2	27 ± 2	8 ± 1	1×10^{-4}
3.56	12 ± 2	26 ± 2	7 ± 1	9×10^{-5}
3.52	12 ± 2	25 ± 2	6 ± 1	6×10^{-5}
3.48	12 ± 2	26 ± 2	6 ± 1	5×10^{-5}
3.44	12 ± 2	40 ± 4	22 ± 1	2×10^{-4}
3.40	12 ± 3	63 ± 4	39 ± 2	1×10^{-4}
3.36	10 ± 3	73 ± 4	44 ± 1	1×10^{-4}
3.32	8 ± 2	82 ± 3	49 ± 2	1×10^{-4}
3.28	7 ± 2	90 ± 3	53 ± 2	1×10^{-4}
3.24	6 ± 2	95 ± 2	54 ± 1	1×10^{-4}
3.20	6 ± 1	99 ± 2	56 ± 1	8×10^{-5}
3.16	6 ± 2	102 ± 2	58 ± 2	1×10^{-4}
3.12	6 ± 1	105 ± 2	59 ± 1	8×10^{-5}
3.08	7 ± 2	107 ± 2	60 ± 2	9×10^{-5}
3.04	7 ± 2	109 ± 3	62 ± 2	1×10^{-4}
3.00	8 ± 2	111 ± 3	64 ± 2	1×10^{-4}
2.96	10 ± 3	105 ± 6	71 ± 4	1×10^{-4}
2.92	10 ± 3	107 ± 7	77 ± 5	3×10^{-4}
2.88	10 ± 3	107 ± 8	81 ± 6	3×10^{-4}
2.84	11 ± 3	108 ± 8	84 ± 6	3×10^{-4}
2.80	11 ± 3	110 ± 9	85 ± 7	3×10^{-4}
2.76	12 ± 4	110 ± 9	94 ± 7	3×10^{-4}
2.72	12 ± 4	111 ± 10	97 ± 8	3×10^{-4}
2.68	12 ± 4	111 ± 10	102 ± 9	3×10^{-4}
2.64	11 ± 3	114 ± 10	108 ± 10	3×10^{-4}
2.60	11 ± 3	116 ± 10	110 ± 11	3×10^{-4}
2.56	12 ± 4	116 ± 10	117 ± 12	3×10^{-4}
2.52	12 ± 4	116 ± 11	118 ± 13	3×10^{-4}
2.48	10 ± 3	118 ± 8	109 ± 7	2×10^{-4}
2.44	17 ± 4	111 ± 10	111 ± 8	2×10^{-4}
2.40	17 ± 2	111 ± 11	119 ± 9	2×10^{-4}
2.36	9 ± 2	123 ± 8	117 ± 8	2×10^{-4}
2.32	20 ± 3	111 ± 7	116 ± 6	8×10^{-5}
2.28	19 ± 3	115 ± 7	116 ± 6	7×10^{-5}
2.24	15 ± 3	120 ± 7	124 ±7	9×10^{-5}
2.20	20 ± 3	115 ± 8	125 ± 7	1×10^{-4}
2.16	23 ± 3	113 ± 8	126 ± 7	1×10^{-4}
2.12	16 ± 3	125 ± 7	123 ± 7	7×10^{-5}
2.08	7 ± 1	139 ± 4	127 ± 6	1×10^{-4}
2.04	7 ± 1	141 ± 4	127 ± 6	1×10^{-4}
2.00	12 ± 2	135 ± 6	128 ± 7	7×10^{-5}

Table S5. Contact resistance (R_{cont}), interphase resistance mainly related with lithium SEI and charge transfer (R_{Li}), charge transfer resistance associated with LFMP (R_{ct}), and chi-square value indicating the accuracy (χ^2) of the NLLS [6,7] analysis using the equivalent circuit $R_e(R_{cont}Q_{cont})(R_{Li}Q_{Li})(R_{ct}Q_{ct})$ on the impedance data obtained from SPEIS measurement of the Li|LFMP cell during discharge process. See Fig. 6(c) in the Manuscript for related Nyquist plots.

Fig. S8 shows the DRT function [8] (Fig. S8a) with the related Sum of Squared Residuals (SSR) vs. λ plot (Fig. S8b) of Li|LFMP half-cell (red), and the symmetrical Li|Li (grey) and LFMP|LFMP (green) cells. DRT for the symmetrical cells are calculated to deconvolute the contribution of lithium counter electrode and LFMP. From the peak frequency position and shifts at different temperatures it is possible to isolate the contribution of charge transfer resistance of the LFMP active material from the other contributions, as reported by peak indexing of Fig. S8(a). The calculation of DRT functions is performed according to the optimal λ factor as shown in Fig. S8(b). To further confirm the peak indexing for the different contributions, the Arrhenius plot of the Areal Specific Resistance (ASR) values obtained for all the symmetrical cell processes is provided in Fig. S8(c), with associated coefficient of determination (R^2). As expected, only the fit for R_3 resistance of symmetrical LFMP|LFMP cell (corresponding to *P3* peak), and for R_2 resistance of the symmetrical Li|Li cell (corresponding to *P2* peak) presents linear trend with $R^2 > 0.99$, thus confirming that the associated process is related with charge transfer [9]. See Results and Discussion of Fig. 6 in the Manuscript for details.

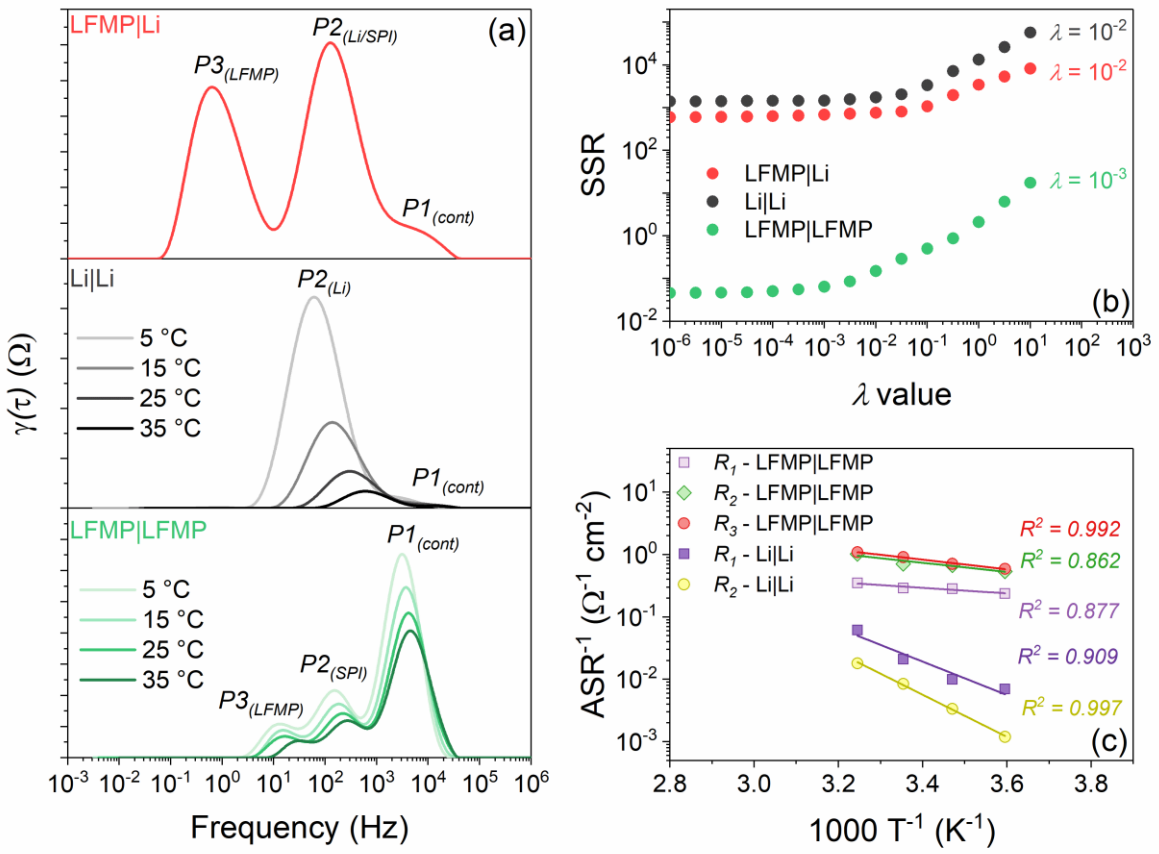

Fig. S8. (a) DRT function [8] with associated peak indexing, and (b) related SSR vs. λ plot for Li|LFMP half-cell (red), Li|Li symmetrical cell (grey), and LFMP|LFMP symmetrical cell (green). DRT for Li|Li and LFMP|LFMP cells obtained at 5 °C, 10 °C, 15 °C, and 25 °C. (c) Arrhenius plot of the ASR for the symmetrical cell processes with associated R^2 values. See Fig. 6 in the Manuscript for discussion.

Fig. S9 depicts the trend of electrolyte resistance (R_e), contact resistance (R_{cont}), lithium resistance (R_{Li}), and LFMP charge transfer resistance (R_{ct}) as function of the LFMP electrode potential, for both de-lithiation and lithiation processes in Li|LFMP cell. Fig. 6(e) in the Manuscript shows the R_{ct} trend in combination with a voltammetry cycle in lithium cell, while Table S4 and Table S5 report corresponding resistance values.

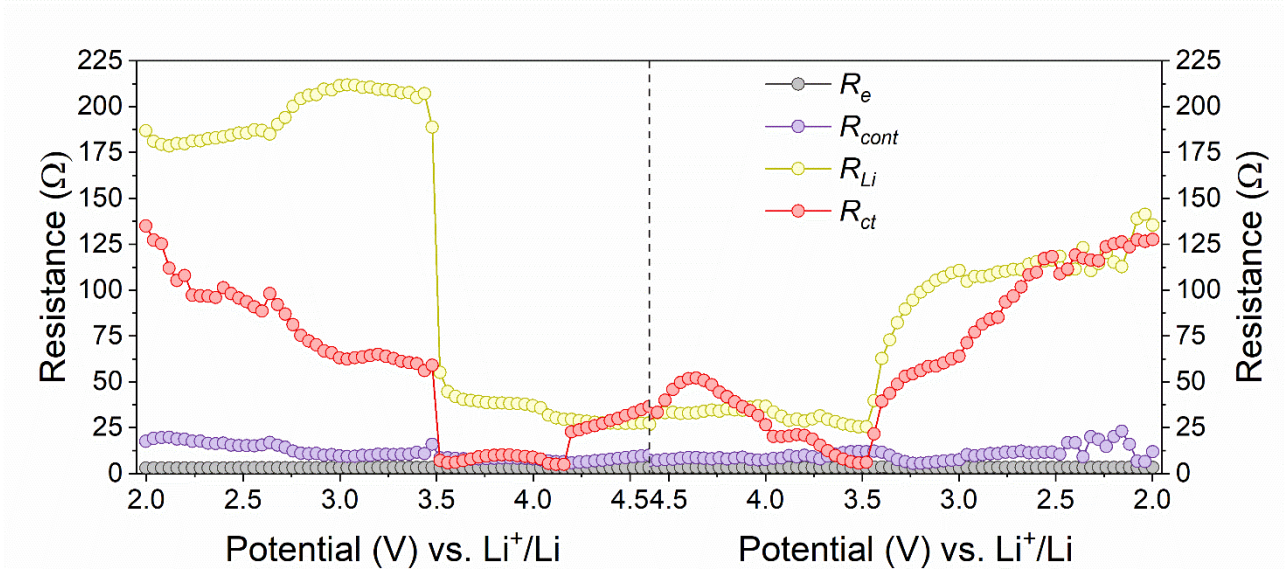

Fig. S9. Trend of R_e (grey), R_{cont} (purple), R_{Li} (yellow), and R_{ct} (red) as a function of potential during de-lithiation (left-side panel) and lithiation (right side panel) of LFMP obtained from NLLS analysis [6,7] of Fig. 6(a) and Fig. 6(c) in the Manuscript. See the Experimental Section in the Manuscript for sample' acronyms and Table S3 and Table S4 for corresponding resistance values.

Fig. S10 reports the Nyquist plots upon de-sodiation (Fig. S10a) and sodiation (Fig. S10b) from the SPEIS analysis of the NFMP electrode performed at the 3rd cycle. The impedance plots are collected every 40 mV in order to evaluate all the electrochemical processes occurring at the interfaces. These spectra are fitted through the NLLS method [6,7] using the RelaxIS3 software focusing on the low-frequency diffusion region which was subtracted for the calculation of DRT. The Nyquist plots without diffusion contributions are reported in Fig. 7 of the Manuscript. The NNLS fit is performed using the equivalent circuit $R_e(R_iQ_i)WQ_w$ including the electrolyte resistance as high-frequency intercept of the plot with the real axis (R_e), in series with three resistances and constant phase elements accounting for the interphase associated to SEI formation and charge transfer of the electrodes (R_iQ_i) semicircles at medium frequency, and a Warburg element in series with solid state diffusion element at low-frequency to simulate both transmissive and reflective boundaries (WQ_w). See the Experimental section and Fig. 7 in the Manuscript for details.

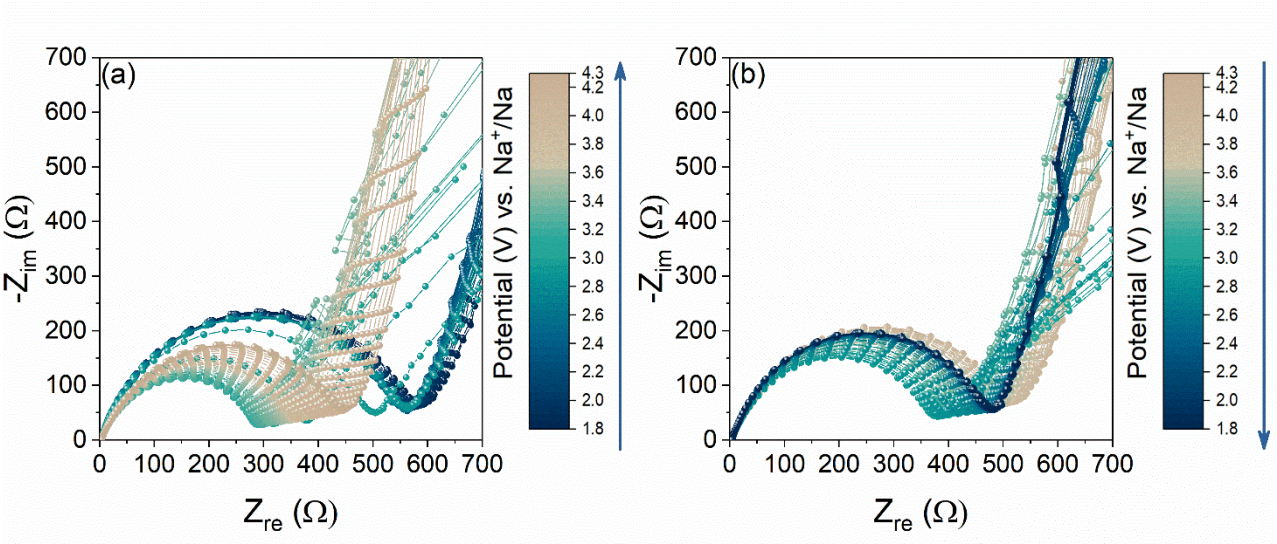

Fig. S10. Nyquist plots obtained during (a) de-sodiation and (b) sodiation from the SPEIS analysis of NFMP electrode performed at the 3rd cycle. EIS collected every 40 mV; potential range: 1.8 – 4.3 V vs. Na^+/Na; frequency range: 200 kHz – 10 mHz; alternate voltage signal: 10 mV. See the Experimental section and Fig. 7 in the Manuscript for the related experiment and data.

The Nyquist plots upon charge and discharge in Fig. 7(a) and Fig. 7(c) in the Manuscript are analyzed by NLLS fitting [6,7] and the results are reported in Table S6 and Table S7, respectively, to obtain the R_{ct} trend associated to the charge transfer resistance of NFMP, as reported in Fig. 7(e) in the Manuscript. The NLLS fits are performed with the equivalent circuit $R_e(R_{cont}Q_{cont})(R_{Na}Q_{Na})(R_{ct}Q_{ct})$ including the electrolyte resistance as high-frequency intercept of the plot with the real axis (R_e), in series with three resistances and constant phase elements accounting for: the contact resistance semicircle at higher frequency, related with cables and particles/current collector contact (R_{cont}); the interphase resistance semicircle at medium-high frequency, related with the SEI and SPI formation at the electrodes and to sodium charge transfer (R_{Na}); and the other interphase resistance semicircle at lower frequency, related with the NFMP charge transfer (R_{ct}).

Potential (V vs. Na^+/Na)	R_{cont} (Ω)	R_{Na} (Ω)	R_{ct} (Ω)	χ^2
1.80	39 ± 7	530 ± 10	128 ± 8	4×10^{-5}
1.84	36 ± 7	530 ± 9	144 ± 8	3×10^{-5}
1.88	33 ± 9	534 ± 12	137 ± 9	5×10^{-5}
1.92	33 ± 11	527 ± 14	148 ± 10	7×10^{-5}
1.96	32 ± 11	531 ± 14	150 ± 10	6×10^{-5}
2.00	31 ± 10	528 ± 13	150 ± 10	6×10^{-5}
2.04	32 ± 11	524 ± 14	149 ± 10	6×10^{-5}
2.08	33 ± 11	516 ± 14	150 ± 10	6×10^{-5}
2.12	30 ± 12	524 ± 15	138 ± 10	6×10^{-5}
2.16	30 ± 12	519 ± 15	135 ± 9	7×10^{-5}
2.20	33 ± 7	518 ± 17	128 ± 9	8×10^{-5}
2.24	49 ± 14	494 ± 19	128 ± 9	5×10^{-5}
2.28	38 ± 5	506 ± 17	125 ± 10	5×10^{-5}
2.32	46 ± 8	498 ± 20	122 ± 9	5×10^{-5}
2.36	48 ± 10	497 ± 22	118 ± 9	6×10^{-5}
2.40	44 ± 6	498 ± 18	113 ± 8	4×10^{-5}
2.44	48 ± 8	495 ± 20	111 ± 10	5×10^{-5}
2.47	48 ± 10	494 ± 22	107 ± 9	5×10^{-5}
2.51	43 ± 9	501 ± 22	103 ± 10	6×10^{-5}
2.55	45 ± 6	495 ± 18	101 ± 8	4×10^{-5}
2.59	47 ± 8	496 ± 20	94 ± 8	4×10^{-5}
2.63	47 ± 9	496 ± 20	96 ± 7	4×10^{-5}
2.67	55 ± 10	484 ± 22	103 ± 9	4×10^{-5}
2.71	55 ± 3	487 ± 24	95 ± 8	5×10^{-5}
2.75	54 ± 3	488 ± 24	96 ± 8	4×10^{-5}
2.79	58 ± 4	485 ± 25	94 ± 8	4×10^{-5}
2.83	57 ± 6	486 ± 27	94 ± 8	5×10^{-5}
2.87	55 ± 7	490 ± 28	90 ± 8	5×10^{-5}
2.91	53 ± 6	491 ± 27	87 ± 8	4×10^{-5}
2.95	39 ± 7	417 ± 8	102 ± 3	1×10^{-5}
2.99	64 ± 3	300 ± 13	38 ± 3	2×10^{-5}
3.03	48 ± 6	260 ± 7	33 ± 2	9×10^{-6}
3.07	40 ± 5	249 ± 5	30 ± 2	1×10^{-5}
3.11	47 ± 3	235 ± 4	28 ± 2	5×10^{-6}
3.15	44 ± 3	237 ± 4	26 ± 2	5×10^{-6}
3.19	45 ± 3	237 ± 3	25 ± 1	4×10^{-6}
3.23	42 ± 5	246 ± 6	28 ± 2	2×10^{-5}
3.27	48 ± 8	242 ± 11	34 ± 3	5×10^{-5}
3.31	47 ± 5	250 ± 7	29 ± 3	2×10^{-5}
3.35	44 ± 3	253 ± 12	46 ± 3	8×10^{-5}
3.39	44 ± 4	268 ± 5	29 ± 2	1×10^{-5}
3.43	44 ± 6	276 ± 7	40 ± 3	3×10^{-5}
3.47	47 ± 6	276 ± 8	36 ± 4	3×10^{-5}
3.51	44 ± 6	287 ± 7	45 ± 3	3×10^{-5}
3.55	46 ± 6	290 ± 7	47 ± 3	3×10^{-5}
3.59	47 ± 5	294 ± 6	48 ± 3	2×10^{-5}
3.63	48 ± 5	297 ± 6	50 ± 3	2×10^{-5}
3.67	49 ± 5	300 ± 6	51 ± 3	2×10^{-5}
3.71	45 ± 7	308 ± 9	49 ± 4	4×10^{-5}
3.75	46 ± 7	308 ± 9	52 ± 4	4×10^{-5}
3.79	48 ± 7	307 ± 9	53 ± 4	4×10^{-5}
3.82	47 ± 7	310 ± 8	53 ± 4	4×10^{-5}
3.86	48 ± 7	314 ± 8	55 ± 4	3×10^{-5}
3.90	49 ± 7	319 ± 8	59 ± 4	3×10^{-5}

3.94	48 ± 6	330 ± 8	60 ± 4	3×10^{-5}
3.98	47 ± 8	341 ± 9	63 ± 4	5×10^{-5}
4.02	48 ± 7	351 ± 9	66 ± 4	4×10^{-5}
4.06	48 ± 7	360 ± 9	69 ± 5	4×10^{-5}
4.10	50 ± 7	366 ± 8	73 ± 5	3×10^{-5}
4.14	49 ± 6	374 ± 8	76 ± 5	3×10^{-5}
4.18	51 ± 6	377 ± 8	80 ± 5	3×10^{-5}
4.22	55 ± 7	377 ± 9	88 ± 6	3×10^{-5}
4.26	53 ± 8	385 ± 12	84 ± 6	5×10^{-5}
4.30	61 ± 3	378 ± 14	91 ± 7	5×10^{-5}

Table S6. Contact resistance (R_{cont}), interphase resistance mainly related with sodium SEI and charge transfer (R_{Na}), charge transfer resistance associated with NFMP (R_{ct}), and chi-square value indicating the accuracy (χ^2) of the NLLS [6,7] analysis using the equivalent circuit $R_e(R_{cont}Q_{cont})(R_{Na}Q_{Na})(R_{ct}Q_{ct})$ on the impedance data obtained from SPEIS measurement of the Na|NFMP cell during charge process. See Fig. 7(a) in the Manuscript for related Nyquist plots.

Potential (V vs. Na^+/Na)	R_{cont} (Ω)	R_{Na} (Ω)	R_{ct} (Ω)	χ^2
4.30	47 ± 8	405 ± 8	94 ± 5	5×10^{-5}
4.26	44 ± 8	424 ± 9	108 ± 6	6×10^{-5}
4.22	44 ± 8	433 ± 8	120 ± 6	5×10^{-5}
4.18	44 ± 7	443 ± 8	129 ± 6	5×10^{-5}
4.14	44 ± 7	452 ± 8	136 ± 6	5×10^{-5}
4.10	44 ± 7	455 ± 8	137 ± 6	6×10^{-5}
4.06	44 ± 8	461 ± 8	137 ± 7	6×10^{-5}
4.02	44 ± 8	467 ± 8	135 ± 6	6×10^{-5}
3.98	43 ± 8	471 ± 8	130 ± 7	7×10^{-5}
3.94	43 ± 8	472 ± 9	125 ± 7	7×10^{-5}
3.90	43 ± 9	474 ± 9	120 ± 7	8×10^{-5}
3.86	42 ± 9	474 ± 9	113 ± 6	8×10^{-5}
3.82	43 ± 9	471 ± 9	110 ± 7	9×10^{-5}
3.79	45 ± 8	462 ± 8	114 ± 6	6×10^{-5}
3.75	46 ± 8	456 ± 8	109 ± 6	6×10^{-5}
3.71	45 ± 8	454 ± 8	103 ± 6	6×10^{-5}
3.67	45 ± 8	448 ± 8	100 ± 6	7×10^{-5}
3.63	45 ± 8	441 ± 9	97 ± 6	7×10^{-5}
3.59	45 ± 8	434 ± 9	92 ± 5	7×10^{-5}
3.55	45 ± 9	425 ± 9	89 ± 5	7×10^{-5}
3.51	44 ± 9	417 ± 9	86 ± 5	7×10^{-5}
3.47	44 ± 9	407 ± 10	84 ± 5	7×10^{-5}
3.43	43 ± 9	398 ± 10	82 ± 5	7×10^{-5}
3.39	43 ± 2	389 ± 10	81 ± 5	7×10^{-5}
3.35	42 ± 2	381 ± 11	79 ± 5	8×10^{-5}
3.31	41 ± 2	372 ± 11	71 ± 4	7×10^{-5}
3.27	42 ± 2	368 ± 12	63 ± 5	7×10^{-5}
3.23	42 ± 2	358 ± 11	55 ± 4	7×10^{-5}
3.19	44 ± 2	350 ± 11	48 ± 4	6×10^{-5}
3.15	45 ± 9	341 ± 10	44 ± 4	5×10^{-5}
3.11	46 ± 9	333 ± 9	39 ± 3	4×10^{-5}
3.07	44 ± 9	330 ± 9	35 ± 3	4×10^{-5}
3.03	46 ± 9	323 ± 9	36 ± 3	4×10^{-5}
2.99	45 ± 9	324 ± 9	38 ± 3	3×10^{-5}

2.95	45 ± 8	326 ± 8	40 ± 3	3×10^{-5}
2.91	44 ± 7	330 ± 8	30 ± 4	3×10^{-5}
2.87	40 ± 8	347 ± 8	33 ± 4	3×10^{-5}
2.83	36 ± 9	374 ± 11	39 ± 5	5×10^{-5}
2.79	34 ± 9	390 ± 9	42 ± 4	4×10^{-5}
2.75	35 ± 9	401 ± 9	45 ± 5	4×10^{-5}
2.71	34 ± 8	408 ± 9	47 ± 5	4×10^{-5}
2.67	32 ± 8	420 ± 11	61 ± 5	5×10^{-5}
2.63	32 ± 8	424 ± 10	62 ± 5	5×10^{-5}
2.59	35 ± 4	427 ± 14	61 ± 5	1×10^{-4}
2.55	35 ± 4	425 ± 13	63 ± 5	9×10^{-5}
2.51	35 ± 4	428 ± 13	63 ± 6	1×10^{-4}
2.47	35 ± 4	428 ± 13	63 ± 5	9×10^{-5}
2.44	37 ± 4	427 ± 13	66 ± 6	1×10^{-4}
2.40	36 ± 4	428 ± 13	67 ± 5	9×10^{-5}
2.36	37 ± 4	430 ± 13	69 ± 6	9×10^{-5}
2.32	34 ± 5	434 ± 14	65 ± 5	1×10^{-4}
2.28	35 ± 5	436 ± 14	65 ± 5	1×10^{-4}
2.24	34 ± 4	438 ± 14	67 ± 5	1×10^{-4}
2.20	34 ± 5	440 ± 14	68 ± 6	1×10^{-4}
2.16	35 ± 4	434 ± 13	71 ± 5	9×10^{-5}
2.12	35 ± 4	437 ± 14	70 ± 5	9×10^{-5}
2.08	35 ± 4	433 ± 13	75 ± 5	8×10^{-5}
2.04	33 ± 6	444 ± 15	72 ± 6	1×10^{-4}
2.00	34 ± 6	441 ± 15	75 ± 6	1×10^{-4}
1.96	33 ± 6	441 ± 15	74 ± 6	1×10^{-4}
1.92	34 ± 5	435 ± 15	79 ± 6	1×10^{-4}
1.88	33 ± 6	442 ± 15	76 ± 6	1×10^{-4}
1.84	33 ± 6	441 ± 15	79 ± 5	1×10^{-4}
1.80	30 ± 5	444 ± 14	78 ± 6	1×10^{-4}

Table S7. Contact resistance (R_{cont}), interphase resistance mainly related with sodium SEI and charge transer (R_{Na}), charge transfer resistance associated with NFMP (R_{ct}), and chi-square value indicating the accuracy (χ^2) of the NLLS [6,7] analysis using the equivalent circuit $R_e(R_{cont}Q_{cont})(R_{Na}Q_{Na})(R_{ct}Q_{ct})$ on the impedance data obtained from SPEIS measurement of the Na|NFMP cell during discharge process. See Fig. 7(c) in the Manuscript for related Nyquist plots.

Fig. S11 shows the DRT function [8] (Fig. S11a) with the related SSR vs. λ plot (Fig. S11b) of Na|NFMP half-cell (blue), and the symmetrical Na|Na (grey) and NFMP|NFMP (green) cells. DRT for the symmetrical cells are calculated to deconvolute the contribution of sodium counter electrode and NFMP. From the peak frequency position and shifts at different temperatures it is possible to isolate the contribution of charge transfer resistance of the NFMP active material from the other contributions, as reported by peak indexing of Fig. S11(a). The calculation of DRT functions is performed according to the optimal λ factor as shown in Fig. S11(b). To further confirm the peak indexing for the different contributions, the Arrhenius plot of the ASR values obtained for all the symmetrical cell processes is provided in Fig. S11(c), with associated R^2. As expected, only the fit for R_3 resistance of symmetrical NFMP|NFMP cell (corresponding to *P3* peak), and for R_2 resistance of the symmetrical Na|Na cell (corresponding to *P2* peak) presents a linear trend with $R^2 > 0.99$, thus confirming that the associated process is related with charge transfer [9]. See Results and Discussion of Fig. 7 in the Manuscript for details.

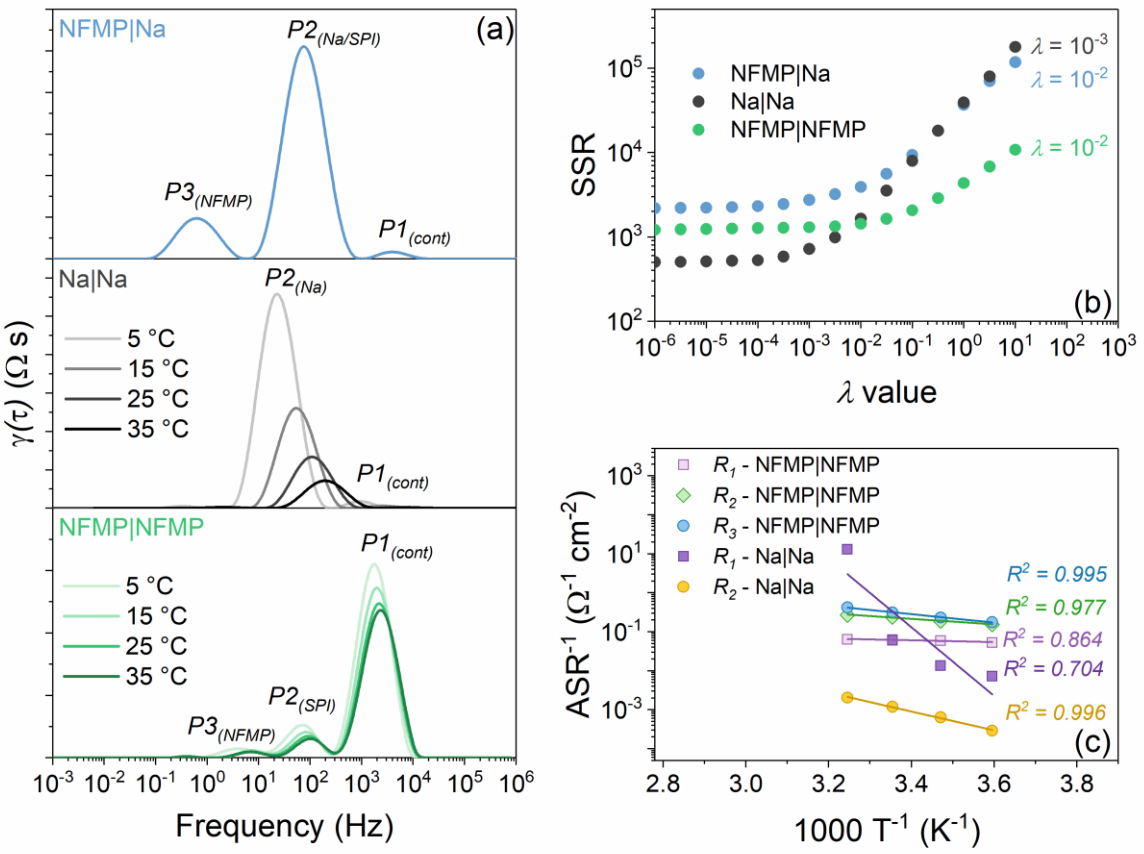

Fig. S11. (a) DRT function [8] with associated peak indexing, and (b) related SSR vs. λ plot for Na|NFMP half-cell (blue), Na|Na symmetrical cell (grey), and NFMP|NFMP symmetrical cell (green). Na|Na and NFMP|NFMP DRT were obtained at 5 °C, 10 °C, 15 °C, and 25 °C. (c) ASR values for the symmetrical cell processes with associated R^2. See Fig. 7 in the Manuscript for discussion.

Fig. S12 depicts the trend of electrolyte resistance (R_e), contact resistance (R_{cont}), sodium resistance (R_{Na}), and NFMP charge transfer resistance (R_{ct}) as function of the NFMP electrode potential in Na|NFMP cell, for both de-sodiation and sodiation processes. Fig. 7(e) in the Manuscript shows the R_{ct} trend during a voltammetry cycle, while Table S6 and Table S7 report corresponding resistance values.

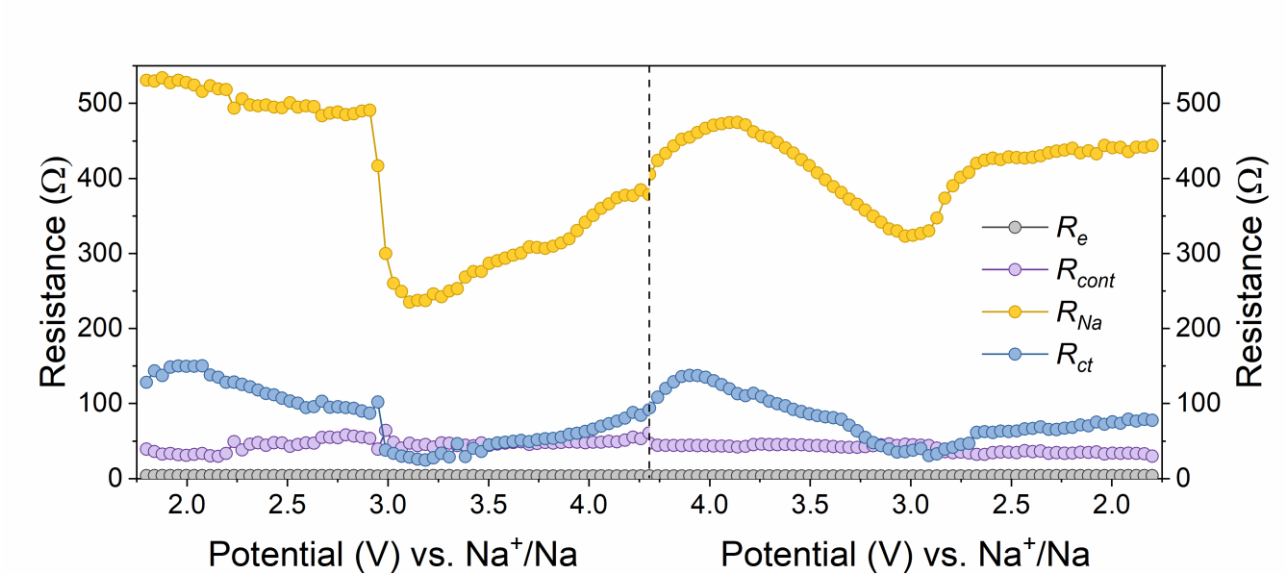

Fig. S12. Trend of R_e (grey), R_{cont} (purple), R_{Na} (yellow), and R_{ct} (blue) as a function of potential during de-sodiation (left-side panel) and sodiation (right side panel) of NFMP obtained from NLLS analysis [6,7] of Fig. 7(a) and Fig. 7(c) in the Manuscript. See Table S5 and Table S6 for corresponding resistance values.

References

[1] L. Minnetti, V. Marangon, J. Hassoun, Adv Sustain Syst 6 (2022) 2100464.

[2] D. Saurel, M. Giner, M. Galceran, J. Rodríguez-Carvajal, M. Reynaud, M. Casas-Cabanas, Electrochim Acta 425 (2022) 140650.

[3] S. Jana, G. Lingannan, M. Ishtiyak, G. Panigrahi, A. Sonachalam, J. Prakash, Mater Res Bull 126 (2020) 110835.

[4] P.B. Moore, Am. Min. 57 (1972) 1333–1344.

[5] V. Marangon, C. Hernández-Rentero, M. Olivares-Marín, V. Gómez-Serrano, Á. Caballero, J. Morales, J. Hassoun, ChemSusChem 14 (2021) 3333–3343.

[6] B. Boukamp, Solid State Ion 20 (1986) 31–44.

[7] B. Boukamp, Solid State Ion 18–19 (1986) 136–140.

[8] F. Ciucci, C. Chen, Electrochim Acta 167 (2015) 439–454.

[9] J.P. Schmidt, T. Chrobak, M. Ender, J. Illig, D. Klotz, E. Ivers-Tiffée, J Power Sources 196 (2011) 5342–5348.